region reflects two anisotropic layers, both with φ oriented parallel to spreading. The upper layer, above a depth of about 100 km, is dominated by spreading-induced flow, which produces no splitting near the axis, where flow is predominantly vertical, but contributes to off-axis splitting as the flow diverges to a predominantly horizontal direction. The lower layer on the Pacific side consists of material experiencing return flow toward the ridge, but comparable return flow is more modest or absent on the Nazca side. Such an asthenospheric return flow could account for the 1-s splitting times seen on the rise axis, because the SKS phases in this study from sources to the west and northwest (Table 1) may sample the anisotropy induced by this flow at depths greater than 100 km.

REFERENCES AND NOTES

1. MELT Seismic Team, *Science* **280**, 1215 (1998).
2. L. P. Vinnik, R. Kind, G. L. Kosarev, L. I. Makeyeva, *Geophys. J. Int.* **99**, 549 (1989).
3. P. G. Silver and W. W. Chan, *J. Geophys. Res.* **96**, 16429 (1991).
4. SKS is a phase that propagates downward from the source as an S wave, converts to a P wave at the core-mantle boundary, travels through the fluid outer core, and then converts back to an S wave at the core-mantle boundary nearer to the point beneath the receiver. (An SKKS phase differs from SKS only in that the core path involves one underside reflection at the core-mantle boundary.) The conversion to P in the outer core removes any splitting accrued along the source side of the path, so when SKS or SKKS converted shear wave is polarized in the direction radial to the source. Several lines of evidence [for example, C. Meade, P. G. Silver, S. Kaneshima, *Geophys. Res. Lett.* **22**, 1293 (1995)] suggest that neither Earth's lower mantle nor the transition zone between the upper and lower mantle contributes substantially to SKS or SKKS splitting. The dominant contribution to such splitting is the preferential alignment of the orthorhombic mineral olivine in the upper mantle beneath the receiving seismometer.
5. For a single anisotropic layer, the delay time will be $\delta t = L \, \delta\beta/\beta_0$, where L is the path length through the anisotropic material and is approximately equal to the layer thickness for near-vertically traveling SKS phases, and β_0 is the isotropically averaged shear velocity. $\delta\beta$ is the dimensionless anisotropy (the difference between the fast and slow shear velocities divided by β_0) and varies as a function of propagation direction ($100 \, \delta\beta$ is the percent anisotropy). Although the interpretation of shear-wave splitting measurements is generally made under the assumption of a single layer of anisotropic material, the more complicated case of multiple layers yields apparent splitting parameters that are functions of the anisotropy characteristics of individual layers [P. G. Silver and M. K. Savage, *Geophys. J. Int.* **119**, 949 (1994)]. Because the SKS and SKKS phases of our study sample only two back azimuths (Table 1), we cannot discount the possibility that there are multiple layers of distinct anisotropy, but the simple spreading-parallel splitting in Fig. 3 argues against such complexity.
6. N. I. Christensen, *Geophys. J. R. Astron. Soc.* **76**, 89 (1984).
7. J.-M. Kendall, *Geophys. Res. Lett.* **21**, 301 (1994).
8. D. K. Blackman *et al.*, *Geophys. J. Int.* **127**, 415 (1996); D. K. Blackman and J.-M. Kendall, *Philos. Trans. R. Soc. London Ser. A* **355**, 217 (1997).
9. In models of passive flow, viscous drag from the separating plates induces a broad zone, 100 km or more in width, of upwelling and melting centered beneath the rise axis. In models of dynamic flow, the buoyancy from retained melt and the depleted mantle residuum, as well as a lower viscosity within the upwelling region, focus upwelling and melting within a narrower zone. See (8) for examples of these models.
10. C. J. Wolfe and P. G. Silver, *J. Geophys. Res.* **103**, 749 (1998).
11. D. R. Toomey *et al.*, *Science* **280**, 1224 (1998).
12. C. DeMets, R. G. Gordon, D. F. Argus, S. Stein, *Geophys. J. Int.* **101**, 425 (1990); *Geophys. Res. Lett.* **21**, 2191 (1994).
13. In the MELT Experiment, the horizontal seismometers were oriented on the basis of seafloor observations of seismic phases other than those utilized here (11); typical standard errors are 10°. Because we minimize the smaller eigenvalue of the covariance matrix of particle motion in solving for the SKS polarizations, small misorientations of the horizontals will map directly into a misorientation of φ but will not affect δt.
14. D. Mainprice and P. G. Silver, *Phys. Earth Planet. Inter.* **78**, 257 (1993).
15. D. W. Forsyth, S. C. Webb, L. M. Dorman, Y. Shen, *Science* **280**, 1235 (1998). Although models that would satisfy both the Rayleigh-wave results and shear-wave splitting are nonunique, the magnitude of Rayleigh-wave azimuthal anisotropy can be used to infer an upper bound on the contribution to splitting from the shallow mantle, because the splitting directions φ are consistently parallel to spreading across the MELT network. If both Rayleigh-wave anisotropy and splitting were caused by anisotropy in a single shallow (<100 km in depth) layer in which olivine a axes were aligned parallel to the spreading direction, then Rayleigh waves would display high azimuthal anisotropy despite the effects of the larger Fresnel zone and path averaging.
16. J. Phipps Morgan and W. H. F. Smith, *Nature* **359**, 524 (1992).
17. M. K. McNutt and A. V. Judge, *Science* **248**, 969 (1990).
18. J. R. Cochran, *Geophys. J. R. Astron. Soc.* **87**, 421 (1986).
19. D. S. Scheirer, D. W. Forsyth, M.-H. Cormier, K. C. Macdonald, *Science* **280**, 1221 (1998).
20. A. E. Gripp and R. G. Gordon, *Geophys. Res. Lett.* **17**, 1109 (1990).
21. Supported by NSF under grants OCE-9402991 to the Department of Terrestrial Magnetism and OCE-9403697 to the Woods Hole Oceanographic Institution (WHOI). This is WHOI contribution 9711.

Mantle Discontinuity Structure Beneath the Southern East Pacific Rise from *P*-to-*S* Converted Phases

Yang Shen,* Anne F. Sheehan, Kenneth G. Dueker, Catherine de Groot–Hedlin, Hersh Gilbert

Receiver functions derived from teleseismic body waves recorded by ocean-bottom seismometers on the southern East Pacific Rise reveal shear waves converted from compressional waves at the mantle discontinuities near 410- and 660-kilometer depth. The thickness of the mantle transition zone between the two discontinuities is normal relative to the global average and indicates that upwelling beneath the southern East Pacific Rise is not associated with an excess temperature in the mantle transition zone.

The deep structure beneath mid-ocean ridges has been a subject of much debate and has direct implications for the mechanism of mantle upwelling beneath ridges as well as the pattern of global mantle circulation. Tomography studies by Su *et al.* (1) have suggested that slow seismic velocities, and hence anomalously warm mantle, exist to depths of 300 km and perhaps greater beneath mid-ocean ridges. This result implies that ridges are the product of deep-mantle upwelling associated with excess temperatures. Convection models that incorporate a platelike lithosphere predict that upwelling beneath ridges entrains

Y. Shen, Department of Geology and Geophysics, Woods Hole Oceanographic Institution, Woods Hole, MA 02543, USA.
A. F. Sheehan, K. G. Dueker, H. Gilbert, Cooperative Institute for Research in Environmental Sciences (CIRES), University of Colorado, Boulder, CO 80309, USA.
C. de Groot–Hedlin, Scripps Institute of Oceanography, La Jolla, CA 92093, USA.

*To whom correspondence should be addressed: E-mail: yshen@whoi.edu

anomalously hot material from a thermal boundary layer either at the core-mantle boundary or at the base of the upper mantle (2). However, surface wave tomographic images constructed by Zhang and Tanimoto (3) indicate that mid-ocean ridges are shallow features, and hence the product of passive upwelling. The lack of a deep-ridge signature is consistent with models in which a low-viscosity asthenosphere acts to decouple upwelling beneath the ridge from flow in the deep mantle (4).

Lateral temperature variations in the upper mantle can be inferred from the depths of seismic discontinuities found on a worldwide basis near 410 and 660 km (5–9). The 410-km discontinuity has been identified with the transition from the α to β phase of $(Mg,Fe)_2SiO_4$ and the 660-km discontinuity with the transition from γ-$(Mg,Fe)_2SiO_4$ to perovskite plus magnesiowustite (10). The depths to the 410- and 660-km phase boundaries, respectively, increase and decrease with higher temperatures. Excess tempera-

tures in the mantle transition zone at either 410- or 660-km depth or both are expected to result in a reduction in transition zone thickness. Here, we report observations of *P*-to-*S* conversions from the 410- and 660-km discontinuities (*P410s* and *P660s*; *Pds* denotes a *P*-to-*S* conversion at depth *d*) beneath the southern East Pacific Rise (SEPR). An anomalously short interval between the *P*-to-*S* converted phases from the 410- and 660-km discontinuities is indicative of a narrow transition zone, suggesting the presence of deep, thermal upwelling; a normal interval indicates the absence of excess temperatures in the transition zone.

The data we used are receiver functions (*11*) derived from teleseismic body waves recorded by 21 of the Mantle Electromagnetic and Tomography (MELT) (*12*) ocean-bottom seismometers (OBSs) on the SEPR (Fig. 1). A range of parameters and procedures in the calculation of OBS receiver functions were tested with synthetic waveforms calculated by a reflectivity method (*13*). Noise from MELT records was added to synthetic waveforms in some tests. We found that filtering designed to suppress water reverberations before the deconvolution in the calculation of receiver functions helped to stabilize the deconvolution (*14*) and to isolate *P*-to-*S* conversions

Fig. 2. (A) Synthetic radial receiver function calculated with reflectivity waveforms for ocean-bottom teleseismic records. The velocity structure is the *iasp91* mantle, a 6-km-thick oceanic crust and a 3-km-thick water layer. The synthetic reflectivity waveforms for an impinging *P* wave with a ray parameter of 0.0573 s/km have been filtered before the deconvolution in the calculation of the receiver function (*14*) to suppress the effect of water reverberations. The amplitude of the receiver function is normalized by the amplitude of the *P* arrival on the radial component. **(B)** Linear stack of MELT radial receiver functions and its 95% confidence limits estimated by a bootstrap method (*17*). The effects of shear-wave splitting and local velocity heterogeneity have been removed. **(C)** An *n*-th root stack of MELT receiver functions (*n* = 3) and its 95% confidence limits. **(D)** Two *n*-th root stacks of MELT receiver functions having horizontal distances of the piecing points of *Pds* ray paths within 300 (top) and 200 (bottom, Fig. 1) km of the ridge axis. The traces have been shifted vertically for clarity.
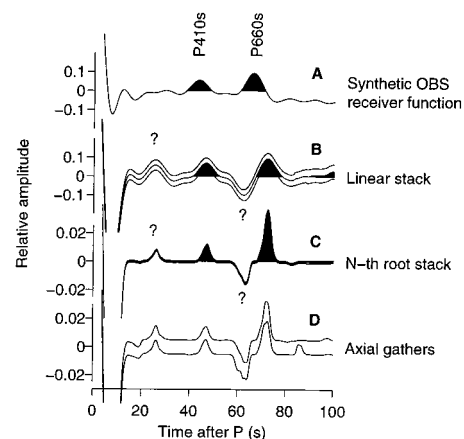
from mantle discontinuities (Fig. 2A). We also found that stacking of receiver functions from different water depths tended to suppress water reverberations, which are offset in time.

We used a total of 89 pairs of radial and transverse receiver functions from records of 10 earthquakes ranging from magnitude *Ms* 6.6 to 8.1 and epicentral distance of 32° to 146°. In addition to receiver functions derived from the wavetrain of direct *P*, we constructed 32 receiver functions from *PP* coda. In the following, for simplicity, we make no further distinction between *P* and *PP*.

We corrected *P* and *Pds* times for lateral velocity heterogeneity and *Pds* times for shear-wave splitting (*15*) and then stacked the corrected radial receiver functions to a reference ray parameter of 0.0573 s/km along theoretical *Pds* moveouts calculated with the velocity structure of the upper mantle beneath 0- to 4-million-year-old Pacific seafloor (*16*). The stacked receiver

function reveals phases in the time windows expected for the 410- and 660-km discontinuities as well as a phase at 25 s after *P* and a negative polarity phase near 62 s (Fig. 2B). The amplitudes of the phases exceed uncertainties due to random noise estimated by a bootstrap method (*17*). Stacking along reverberation moveouts does not yield phases of the same magnitude as those interpreted as *P410s* and *P660s*, indicating that the identified *P410s* and *P660s* are not reverberations from shallower mantle structure. Although the 25-s phase could correspond to a shallow mantle discontinuity near 220-km depth as documented in other regions (*18*), the negative 62-s phase is puzzling. Receiver functions from Iceland, another oceanic upwelling region, show similar large-amplitude, negative arrivals between *P410s* and *P660s* (*5*), although the negative arrivals are not as laterally coherent as *P410s* and *P660s*.

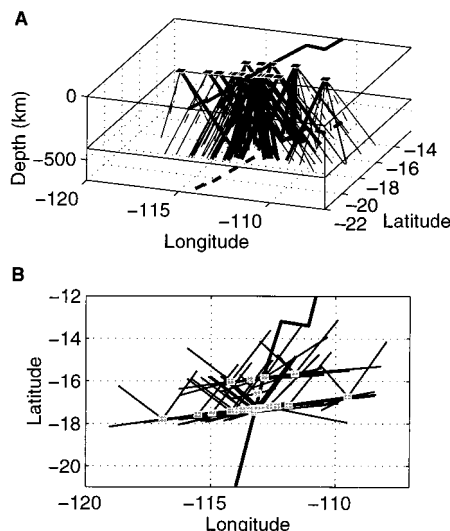Further improvement in arrival signature is achieved (Fig. 2C) with an *n*-th root

Fig. 1. (A) Theoretical ray paths of *P*-to-*S* conversions from the 410- (dashed) and 660-km (solid) discontinuities to 21 of the MELT ocean-bottom seismometers (filled squares). The East Pacific Rise is represented by the thick lines on the seafloor and projected on the 660-km discontinuity as dashed lines. *P660s* ray paths with piercing points within 200 km of the ridge axis at the 660-km discontinuity are shown as thick lines. A total of 89 pairs of radial and transverse receiver functions sample the 410- and 660-km discontinuities within about 650 km of the ridge axis. **(B)** Map view of the *P660s* raypaths from the piercing points at the 660-km discontinuity to the stations.

Fig. 3. Comparison of *P660s* and *P410s* arrival times from this and other studies. Data shown are arrival times with estimated uncertainties less than 1.0 s for the SEPR (×), Iceland (●) (*5*), and a range of continental stations (+) (*7, 8*) and Pacific island stations (○) (*9*). (■) The predicted times for the *iasp91* average Earth model. The line shown has a slope of 1 and satisfies the predicted times for the *iasp91* model (*20*). Variations in the *P410s* and *P660s* times along the line of unit slope are contributed by mantle structure above 410-km depth where the two phases have nearly identical paths. The offsets between the data points and the line of unit slope or the differential *P660s-P410s* times provide information on the thickness of the mantle transition zone. A 1-s change in differential *P660s-P410s* time is equivalent to about a 10-km change in the transition zone thickness, and about a 75-K change in temperature in the mantle transition zone for recent estimates of Clapeyron slopes for the 410- and 660-km discontinuities (*29*).
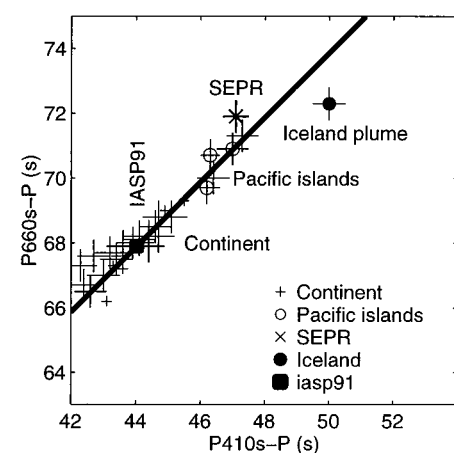
stacking process (*19*), a nonlinear method that reduces apparent periods of the converted phases. The bootstrap estimates of the *P410s* and *P660s* times in the *n*-th root stack (Fig. 2C) are 47.1 ± 0.4 s and 71.9 ± 0.5 s, respectively, similar to the estimates in the linear stack (47.1 ± 1.0 s and 71.7 ± 0.6 s, respectively). The differential *P660s-P410s* time is 24.7 ± 0.6 s in the *n*-th root stack, comparable to that predicted by the *iasp91* (*20*) global earth model (23.9 s). The stacks of receiver functions having horizontal distances of the piercing points of *Pds* ray paths within 300 and 200 km of the ridge axis (Fig. 2D) also yield normal *P660s-P410s* differential times (24.6 ± 0.6 s and 24.7 ± 0.7 s, respectively).

We performed a test of the receiver function stacks by systematically eliminating receiver functions of each earthquake from the gather. Such bootstrapped stacks have similar waveforms (including the negative-polarity phase preceding *P660s*) and *P660s-P410s* differential times, indicating that our results are not overly dependent on any one of the earthquakes we used. We also carried out tests (*21*) which indicate that a possible anisotropic upper-mantle transition zone as reported elsewhere (*22*) has little effect on the *P660s-P410s* differential times in the stacks because of a broad range of back azimuths of the receiver functions (Fig. 1).

The SEPR *P410s* and *P660s* times are compared with those from other regions in Fig. 3. The SEPR *P410s* and *P660s* times, which have been corrected with *P* and *S* delays with zero means across the array (*15*), are greater than those from continental stations (*7*, *8*), less than the Iceland times (*5*), and comparable to those from Pacific islands (*9*). Removing the effects of water depth (3 km) and crustal thickness (6 km) on *Pds* travel times increases the SEPR times by about 0.8 s. The delay of the observed SEPR arrival times relative to *iasp91* can be attributed to a -4 to -5% average *S*-wave velocity anomaly in the upper 410-km mantle, assuming an empirical linear scaling relation between relative perturbations in *P* and *S* velocities (*23*). The magnitude of the velocity anomaly would double if the anomaly is limited in the upper 200 km.

The SEPR *P410s* and *P660s* times are slightly above, but within the uncertainty of, the line of unit slope, indicating that the thickness of the mantle transition zone beneath the SEPR is unlikely to be significantly ($\sim$10 km) less than the global average (*24*) and in *iasp91*. To test the lateral resolution of the stacks, we calculated synthetic *P660s* waveforms (*25*) from a ridge-shaped 660-km discontinuity centered beneath the ridge axis, which has a range of the width (*wid*) and maximum amplitude

(*amp*) of the relief. We stacked the synthetic *P660s* waveforms using different binning width following the same procedures as for the real data. For a binning width of 400 km, we can retrieve significant ($\sim$7 km) depth variation from an anomaly with *amp* = 10 km and *wid* > 400 km or from an anomaly with *amp* = 15 km and *wid* > 300 km. We cannot rule out, however, the possibility that the center of an anomaly of similar dimensions is shifted significantly (>300 km) off-axis or the possibility that the width of upwelling is much less than 300 km for an anomaly with 10- to 15-km relief, because of decreasing number of *Pds* ray paths and increasing uncertainties off-axis and in narrower axial bins.

Additional evidence of a normal transition zone thickness beneath spreading centers comes from receiver functions from Iceland, which show no signature of the Mid-Atlantic Ridge near Iceland in variations of the transition zone thickness (*5*). Furthermore, precursors of *SS* waves with bounce points sampling the northern East Pacific Rise (*26*) show no significant difference in 410- and 660-km discontinuity depths beneath sea floor younger than 10 million years and those beneath older sea floor.

In conclusion, the average transition zone thickness beneath the MELT region is normal relative to the global average for the observed *P410s* and *P660s* ($\sim$250 km), suggesting that excess temperatures do not exist in the mantle transition zone beneath the SEPR. This points to either a shallow (<400 km) return flow or a deep (>400 km) but passive mechanism not associated with excess mantle temperatures. The latter, however, is inconsistent with models in which upwelling beneath the ridge extends either to the base of the upper mantle under strongly layered convection scenarios or into the lower mantle under whole-mantle convection scenarios (*2*).

REFERENCES AND NOTES

1. W. Su, R. L. Woodward, A. M. Dziewonski, *Nature* **360**, 678 (1992).
2. S. Zhong and M. Gurnis, *J. Geophys. Res*. **99**, 15903 (1994).
3. Y. Zhang and T. Tanimoto, *Nature* **355**, 45 (1992).
4. D. Turcotte and J. Phipps Morgan, in *Mantle Flow and Melt Generation at Mid-Ocean Ridges*, J. Phipps Morgan, D. K. Blackman, J. M. Sinton, Eds. (American Geophysical Union, Washington, DC, 1993), pp. 155–182.
5. Y. Shen, S. C. Solomon, I. Th. Bjarnason, C. J. Wolfe, *Nature*, in press.
6. C. W. Wicks and M. A. Richards, *Science* **261**, 1424 (1993).
7. K. Stammler *et al*., *Geophys. Res. Lett*. **19**, 1563 (1992).
8. M. G. Bostock, *J. Geophys. Res*. **101**, 8393 (1996).
9. L. Vinnik, S. Chevrot, J. P. Montagner, *Geophys. Res. Lett*. **24**, 1007 (1997).
10. L.-G. Liu, in *The Earth: Its Origin, Structure and Evolution*, M. W. McElhinny, Ed. (Academic Press, San Diego, CA, 1979), pp. 177–202.
11. C. A. Langston, *Bull. Seismol. Soc. Am*. **67**, 713 (1977); T. J. Owens, G. Zandt, S. R. Taylor, *J. Geophys. Res*. **89**, 7783 (1984).
12. D. W. Forsyth *et al*., *Science* **280**, 1235 (1998).
13. B. L. N. Kennett, *Seismic Wave Propagation in Stratified Media* (Cambridge Univ. Press, Cambridge, 1983).
14. *P*-wave reverberations in a water layer about 3 km thick have a two-way travel time of about 4 s and decrease in energy and reverse sign with each multiple. A low-pass filter with a cut-off period greater than twice the reverberation travel time reduces the effect of reverberations in the calculation of receiver functions. The synthetic waveforms and the MELT data have been band pass–filtered (0.013 to 0.08 Hz) before the deconvolution in the calculation of receiver functions. A water level $c = 0.05$ and a Gaussian parameter $a = 0.31$ are used in the deconvolution. See (*11*) for details.
15. There are up to 0.7-s travel time delays for *P*-wave and 2 to 3 s for *S*-wave (*27*) and 1 to 2 s for *SKS*-wave splitting at the MELT stations (*28*). Because *P410s* and *P660s* have steep (10° to 20° from the vertical) incidence angles in the shallow mantle, we use shear-wave splitting parameters derived from *SKS* waves (*28*) to correct radial and transverse receiver functions for the effect of *Pds* propagation through the anisotropic upper mantle, assumed to be above 400-km depth (*21*). To correct, to the first order, for *P* and *Pds* travel time delays due to direction-averaged velocity heterogeneity, we use the average *P* and *S* delays at each station (*27*), assuming that they reflect smoothed velocity heterogeneity in the upper 200 km. The corrected *P*, *P410s*, and *P660s* times are sensitive to the integrated delays in the upper 400 km but not affected by uncertainties in the thickness of the mantle anisotropic layer or the depth range of velocity heterogeneity in the upper 400 km.
16. C. E. Nishimura and D. W. Forsyth, *Geophys. J*. **96**, 203 (1989).
17. B. Efron and G. Gong, *Am. Stat*. **37**, 36 (1983).
18. J. Revenaugh and T. J. Jordan, *J. Geophys. Res*. **96**, 19,781 (1991).
19. E. R. Kanasewich, C. D. Hemmings, T. Alpaslan, *Geophysics* **38**, 327 (1973).
20. B. L. N. Kennett and E. R. Engdahl, *Geophys. J. Int*. **105**, 429 (1991).
21. To test the effect of an anisotropic transition zone on the *P660s-P410s* differential times, we inserted an anisotropic layer between the 410- and 660-km discontinuities. The fast orientation (*a* axis) of the transversely isotropic layer is horizontal and approximately parallel to the spreading direction (110°) and the observed average *SKS* fast axis. The splitting of a *P660s* phase with a ray parameter of 0.06 s/km is about 0.5 s. Synthetic receiver functions are calculated for earthquake-station pairs having the same back azimuths as in the real data (Fig. 1) and stacked. The *P660s-P410s* differential time in such a stack is not significantly different (<0.1 s) from the one for an isotropic transition zone.
22. L. Vinnik and J.-P. Montagner, *Geophys. Res. Lett*. **23**, 2449 (1996).
23. *S* and *P* velocity anomalies are related in $d\ln Vs/d\ln Vp = (Vs/Vp)(\delta t_s/\delta t_p)$ [M. Ritzwoller, G. Masters, F. Gilbert, *J. Geophys. Res*. **93**, 6369 (1988)], where δt_s (2.52 s) and δt_p (0.7 s) are the range of the average *S*- and *P*-wave travel time residuals at the MELT stations (*27*) and *Vs/Vp* is the ratio of the mantle *S*- and *P*-wave velocities in the *iasp91* model (1/1.82).
24. The thickness of the mantle transition zone in the *iasp91* model (250 km) is a reasonable representation of the global average for the observed *P410s* and *P660s*. For comparison, the average transition zone thicknesses obtained from long-period *SS* precursors in both oceanic and continental regions are less than those in *iasp91* by 10 km (M. P. Flanagan and P. M. Shearer, *J. Geophys. Res*., **103**, 2673 (1998)). It remains debatable whether the difference between the average transition zone thickness from *SS* precursors and in *iasp91* (and converted phases) is due to underestimate of deepening of the 660-km discontinuity for any length scale less than 3000 km as determined with *SS* precursors [E. Chaljub and A. Tarantola, *Geophys. Res. Lett*. **24**, 2613 (1997)].

precursors is a more appropriate representation of the transition zone thickness beneath normal oceans, then the mantle transition zone beneath the SEPR is thicker and colder than normal, inconsistent with models of active thermal upwelling.
25. S. van der Lee, H. Paulssen, G. Nolet, *Phys. Earth Planet. Int.* **86**, 147 (1994).
26. D. K. Lee and S. P. Grand, *Geophys. Res. Lett.* **23**, 3369 (1996).
27. D. R. Toomey *et al.*, *Science* **280**, 1224 (1998).
28. C. J. Wolfe, *ibid.*, p. 1230.
29. C. R. Bina and G. Helffrich, *J. Geophys. Res.* **99**, 15853 (1994).
30. We thank the MELT Instrument Teams for their efforts. This research was supported by the U.S. National Science Foundation.

19 February 1998; accepted 17 April 1998

Phase Velocities of Rayleigh Waves in the MELT Experiment on the East Pacific Rise

Donald W. Forsyth,* Spahr C. Webb, LeRoy M. Dorman, Yang Shen

The phase velocities of Rayleigh waves increase more rapidly with distance from the East Pacific Rise (EPR) axis than is predicted by models of conductive cooling of the lithosphere. Low velocities near the axis are probably caused by partial melt at depths of 20 to 70 kilometers in a zone several hundred kilometers wide. The lowest velocities are offset to the west of the EPR. Wave propagation is anisotropic; the fast direction is approximately perpendicular to the ridge, parallel to the spreading direction. Anisotropy increases from a minimum near the axis to 3 percent or more on the flanks.

$\mathbf{R}$ayleigh waves are elastic waves that travel along the surface of Earth. Although the phase velocity of the wave is weakly dependent on the density and compressional velocity of the medium, the primary sensitivity is to the shear wave velocity (*1*). The peak sensitivity of Rayleigh waves to shear velocity is at a depth of about one-third of a wavelength, or 30 to 35 km for a 25-s period wave, for example. The phase velocity at 25 s is an integrated measure of the shear velocity structure in the upper 100 km of the mantle; the strongest response is for depths of 20 to 70 km, which is expected to be the primary melt production zone (*2*, *3*).

Previous studies of Rayleigh and Love surface waves crossing the oceans from distant, teleseismic earthquakes recorded at island and continent stations indicate that phase velocities increase systematically with increasing age of the sea floor (Fig. 1), in agreement with thermal models for cooling of the oceanic lithosphere. The change in average velocity from the youngest sea floor, less than 4 or 5 million years old, to the average velocity in the next age zone, however, is two to three times larger than could be explained by conductive cooling of the mantle and is caused by a zone of anomalously low shear velocities centered at a depth of 40 to 60 km (*4*). Melt fractions of a

few tenths to 5%, depending on the aspect ratio of the melt pockets, are sufficient to explain these anomalous velocities. In young sea floor with normal crustal thicknesses, any area with phase velocities less than about 3.85 km/s at a 25-s period probably is affected by the presence of partial melt. Global teleseismic studies, however, lack the resolution to determine the width of the zone of partial melting or the lowest velocities at the ridge axis. The Mantle Electromagnetic and Tomography (MELT) Experiment was designed to provide spatial resolution that is limited primarily by the physical averaging associated with finite wavelength waves, not by station or event geometry.

Some teleseismic studies have found that Rayleigh waves propagate faster perpendicular to the East Pacific Rise (EPR) (*5*, *6*). This azimuthal anisotropy is attributed to a pattern of flow in the mantle that aligns the *a* axis of olivine crystals perpendicular to the ridge axis. The conclusion that anisotropy is required has been controversial, because there are trade-offs between a simple pattern of anisotropy and a more complicated pattern of heterogeneous, isotropic velocities. In a weakly anisotropic medium, the phase velocity c is expected to be of the form $c(\omega, \psi) = A_0(\omega) + A_1(\omega)\cos 2\psi + A_2(\omega)\sin 2\psi + A_3(\omega)\cos 4\psi + A_4(\omega)\sin 4\psi$, where ω is the frequency, ψ is the azimuth of propagation of the wave, and A_0 and A_4 are velocity coefficients. Theoretical studies indicate that 4ψ variations should be small for Rayleigh waves (*7*), so we neglect them here.

We selected for analysis records (*8*) from 23 earthquakes distributed around the margins of the Pacific. An estimate of the vari-

ation of phase velocity with age in the MELT study area can be obtained from the records of a single event. The magnitude 7.3 event of 21 February 1996 off the coast of northern Peru lies within 1° of the extension of the great circle path along the primary array of ocean bottom seismometers (OBSs). Assuming that the wave is planar and propagating along the great circle path, we combined different subgroups of OBSs to determine the apparent phase velocity along sections of the linear array (Fig. 1). The lowest velocities are found on a subarray straddling the ridge out to an age of about 0.8 million years ago (Ma) on either side, 55 to 60 km from the axis. Average apparent velocities across subarrays confined to sea floor older than 1.5 Ma exceed 3.8 km/s at a 25-s period, suggesting that the dominant effects of melting are present beneath sea floor less than about 2 Ma in age. There is also asymmetry between the eastern and western flanks of the ridge, with slower velocities beneath the western flank at periods less than 40 s. This asymmetry may reverse at periods greater than 40 s, but the statistical significance is questionable.

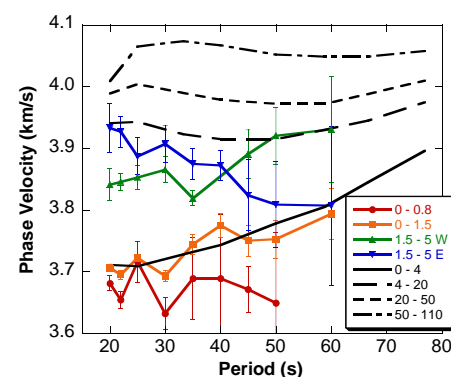To improve the precision and search for anisotropy and along-axis variations in veloc-

D. W. Forsyth, Department of Geological Sciences, Brown University, Providence, RI 02912, USA.
S. C. Webb and L. M. Dorman, Scripps Institution of Oceanography, University of California San Diego, La Jolla, CA 92093, USA.
Y. Shen, Woods Hole Oceanographic Institution, Woods Hole, MA 02543, USA.

*To whom correspondence should be addressed at donald_forsyth@brown.edu

Fig. 1. Apparent phase velocities of Rayleigh waves for a single event along subsections of the primary OBS array (colored symbols) compared with previous teleseismic determinations of average velocities (black lines) as a function of age of the Pacific sea floor (*5*). Legend gives ages of sea floor in millions of years. "W" and "E" indicate west and east of the axis, respectively. Error bars indicate 1 SD. At periods of less than 40 s, note the large jump in velocities from sea floor less than 1.5 Ma in age to that greater than 1.5 Ma, indicating the presence of melt in the upper 100 km beneath very young sea floor.